HHS Public Access

Author manuscript

IEEE Trans Ultrason Ferroelectr Freq Control. Author manuscript; available in PMC 2023 September 01.

Published in final edited form as:

IEEE Trans Ultrason Ferroelectr Freq Control. 2022 September ; 69(9): 2630–2637. doi:10.1109/TUFFC.2022.3192224.

Improving Transcranial Acoustic Targeting: The Limits of CT Based Velocity Estimates and The Role of MR

Taylor D. Webb[*], **Fanrui Fu**[†], **Steven A. Leung**[†], **Pejman Ghanouni**[‡], **Jeremy Dahl**[‡], **Mark D. Does**[§], **Kim Butts Pauly**[*,†,‡]

[*]Department of Biomedical Engineering, University of Utah, Salt Lake City, UT

[†]Department of Bioengineering, Stanford University, Stanford CA

[‡]Department of Radiology, Stanford University, Stanford CA

[§]Department of Radiology, Vanderbilt University, Nashville, TN

Abstract

Transcranial magnetic resonance (MR) guided focused ultrasound (tcMRgFUS) enables the non-invasive treatment of the deep brain. This capacity relies on the ability to focus acoustic energy through the in-tact skull, a feat that requires accurate estimates of the acoustic velocity in individual patient skulls. In current practice, these estimates are generated using a pre-treatment CT scan and then registered to an MR dataset on the day of the treatment. Treatment safety and efficacy can be improved by eliminating the need to register the CT data to the MR images and by improving the accuracy of acoustic velocity measurements. In this study we examine the capacity of MR to supplement or replace CT as a means of estimating velocity in the skull. We find that MR can predict velocity with less but comparable accuracy to CT. We then use micro CT imaging to better understand the limitations of Hounsfield Unit (HU) based estimates of velocity, demonstrating that the macrostructure of pores in the skull contributes to the acoustic velocity of the bone. We find evidence that detailed T2 measurements provide information about pore macrostructure similar to the information obtained with micro CT, offering a potential clinical mechanism for improving patient specific estimates of acoustic velocity in the human skull.

I. Introduction

Transcranial MR guided focused ultrasound (tcMRgFUS) is a noninvasive treatment modality with multiple applications. At the highest intensities, tcMRgFUS can ablate tissue and serves as an alternative to surgery in the treatment of Parkinsonian tremor [1], [2], essential tremor [3], neuropathic pain [4], and obsessive-compulsive disorder [5]. In addition to ablative therapies, tcMRgFUS shows potential for temporary disruption of the blood brain barrier [6]–[10] and for the modulation of neural circuits [11]–[22].

Transcranial acoustic targeting is achieved by registering CT-based estimates of acoustic velocity [23]–[26] to MR images of the brain [27] and simulating the propagation of ultrasound to the intended target. The simulation provides an estimate of the beam aberrations introduced by the skull, enabling the calculation of phase corrections that can be applied to each element of the transducer in order to remove these aberrations. While

this process works well for most patients, some patients must be turned away because the acoustic properties of their skull make it difficult to safely achieve ablative intensities in the thalamus [28]. Improvements in the accuracy with which physicians can predict and correct for the acoustic aberrations introduced by the skull will result in safer and more effective treatments, potentially increasing the number of patients who can benefit from tcMRgFUS.

In this study we first examine the accuracy with which MR imaging can predict acoustic velocity. MR based estimates of acoustic velocity would eliminate the need to acquire and register a pre-treatment CT dataset, streamlining treatments and eliminating a potential source of error. Consistent with Johnson *et al* [29] and Wiesinger *et al* [30], [31] we find a strong correlation between the UTE and ZTE magnitudes and CT HU. Based on the R-squared value, we find that ZTE and UTE magnitude can predict velocity with similar but slightly less accuracy than CT. These results suggest that MR based velocity predictions have the potential to replace CT during treatment planning for some tcMRgFUS procedures.

Second, we explored the role of pore structure in modifying acoustic velocity in skull bone in order to better understand why existing transformations between CT HU and acoustic velocity only account for approximately half of the observed variation in human skull bone [26]. Much is known about bone health from quantitative ultrasound (QUS), which is emerging as a noninvasive way to measure bone strength and structure [32].Simulation of QUS in human femurs and tibia demonstrate that while porosity and bone thickness are the most important indicators of acoustic velocity [33], [34] the size and structure of pores also play a significant role [35], [36].In addition, experimental studies have demonstrated that the acoustic velocity in the femur and tibia is correlated to mechanical strength [37] as well as the micro-structure [38] of pores within the bone.

Since skull imaging for tcMRgFUS has been done with CT and MRI, we explored the role that these modalities can play in determining the relationship between bone microstructure and acoustic velocity. We studied pore structure on micro CT as well as measurements of the MRI T2 signal decay. Our micro CT results demonstrate that pore structure, which is not captured by the clinical HU value, contributes significantly to variations in the acoustic velocity in skull bone. In particular, we find that including measurements of the average pore eccentricity in a fragment yields substantial improvement to the accuracy of velocity predictions. Because the MR signal is sensitive to the micro-environment of the water, blood, marrow and other soft tissue components found in porous bone [39]MR measurements may provide an additional method for measuring variations in pore structure across patient skulls. We thus examined a full reconstruction of the spectrum of T2 signal decay in bone as a predictor of acoustic velocity. We found evidence that differences in the T2 spectrum are predictive of variations in acoustic velocity that are not captured by conventional CT.

II. Methods

A. Sample Preparation

Two *ex-vivo* dried human skulls (60 year old male, 62 year old female) were acquired from Skulls Unlimited. The sample preparation has been described previously [26]. Briefly,

12 mm bores were removed from the skulls and the inner and outer tables and diploë were separated from one another in order to produce more homogeneous samples. The samples were then sanded in order to achieve flat and parallel interfaces. 90 fragments were generated with 48 from the outer table, 31 from the diploë, and 11 from the inner table. In order to more closely approximate *in-vivo* conditions, all fragments were degassed in water in a vacuum chamber. The vacuum pressure was approximately 25 in/Hg and fragments were degassed for a minimum of 12 hours before experiments began.

B. CT Imaging

A prior study [26] showed that the reconstruction algorithms and x-ray energies used to acquire a CT image can have a large impact on the relationship between acoustic velocity and CT HU. The same set of CT images used in that study are used in this work and the reader is referred to that paper for details.

The CT data most relevant to this study are the images acquired on a GE Discovery CT750 [GE, Waukesha, WI] with a bone kernel (commercially known as Bone Plus) and a set of images acquired on the same scanner using a model based iterative reconstruction approach (commercially know as Veo). The Bone Plus configuration matches the setup currently used in the Stanford essential tremor treatments and the Veo configuration yielded the best estimate of velocity in [26]. Bone plus images were acquired at energies of 80, 100, 120, and 140 kVp and Veo images were acquired at energies of 80, 120, and 140 kVp.

Regions of interest were determined for each fragment by automatically thresholding the CT images using Otsu's method [40]. Hole filling [41] was then performed to generate a segmentation of the fragment. The center of the segmented fragment is then selected as the center of a three-dimensional cylinder with a radius and height slightly smaller than the radius and height of the fragment. The final region of interest is the intersection of the cylinder and the segmentation of the fragment. The average HU for each fragment is then taken as the average value within this region of interest.

C. MR Imaging

ZTE images were acquired on a 3 Tesla system [GE, Waukesha, WI] with the product sequence Silenz (TR=200 ms, TE=24 μs, averages=1.6, FOV=18 cm, 6 channel flex coil, slice thickness=0.5 mm, in plane resolution=0.70 mm, flip angle=5°). UTE images were acquired using a center out sequence (TE=32μs, TR=6 ms, FOV=18 cm, 6 channel flex coil, slice thickness=0.7 mm, in-plane resolution=0.63 mm, flip angle=5°). These parameters represent nominal resolution. However, the effective voxel size is larger due to $T2^*$ blurring. In both the UTE and ZTE images GE's large Flex coil was used to acquire the data and coil shading was removed by normalizing the average magnitude in the fragment to the average magnitude in the same region of interest acquired in a 2% agar phantom. Phantom images were acquired immediately after imaging the bone fragments without changing parameters.

The MR images were segmented using a template matching technique. The algorithm generated a cylinder matching the radius and height of the fragment and used cross correlation to determine the optimal location of the template. Once the center of the fragment was determined, a region of interest slightly smaller than the fragment (3 mm

in the radial dimension and twice the in plane resolution in the thickness dimension) was selected as the final region of interest. Fragments that were too thin (their thickness was less than twice the ZTE in-plane resolution - 1.4mm) were excluded from the MR analysis. This choice of ROI limits the impact of partial voluming at the fragment edges. Five fragments (three from the inner table, and one from the outer table and diploë) were excluded in this way.

T2* was estimated using the UTE sequence described above. A T2* value was estimated by fitting the average magnitude in the fragment, measured at 5 echo times, to a single decaying exponential. The 5 echo times were TE = 32, 200, 500, 700, and 900 μs and the repetition time was 10 ms.

A detailed T2 spectra was measured in eight fragments (selected because they had a range of velocities despite having similar HU values) using a Varian 4.7T horizontal bore magnet. To characterize T2, we used a Carr-Purcell-Meiboom-Gill (CPMG) sequence with a total of 30,000 echoes, spaced 100μs apart. More details on the sequence can be found in [39].

D. Micro CT Imaging

The CT dataset was augmented by micro CT (25 micron isotropic resolution) scans of each fragment acquired using a Trifoil CT120 system [Chatsworth, CA]. The micro CT images were segmented using the same template matching technique as the MR images.

Fragment segmentation was performed using ImageJ. After gaussian blurring with $\sigma = 2$ the "Auto local threshold" method with the setting of 'MidGrey' was used to segment out pores from each fragment. The MidGrey method uses the following function

$$\text{pixel} = (\text{pixel} > ((\max + \min)/2) - c) \quad (1)$$

where max and min are the max and min values in the window of 50 pixels radius and c is a constant which equals the mean value of the slice divided by 15. Finally, each pore was separated out in each slice using the "Analyze Particles" method. Pores with an area smaller than 0.01 mm^2 were discarded as we found that many of the pores detected within this range were erroneous.

Each fragment was labeled with an average pore size, porosity, and pore eccentricity. Each parameter is measured in 2D and averaged within each slice and the fragment is then labeled with the average value across all slices. Pore size was defined as the average two dimensional area of each pore across all slices in the region of interest and was measured by counting the pixels in each pore. The porosity was defined as the number of pore pixels in the ROI divided by the total number of pixels in the ROI. Pore eccentricity was measured in two dimensions using MATLAB's regionprops algorithm. The algorithm finds the ellipse that has the same second moment as the pore and then computes the ratio of the distance between the ellipse's foci and the length of its major axis.

E. Acoustic Velocity

The methods used to measure the acoustic velocity are described in [26]. Briefly, an aluminum frame held each sample at the focal spot of a transducer centered at 500 kHz (Olympus, V301, [Tokyo, Japan], focused, 38 mm aperture, 25 mm focal length). The transmitted pulse was recorded by a hydrophone placed behind the fragment. The speed of sound was estimated by measuring the arrival time of a short pulse with and without the bone fragment present in the beam path. The difference in arrival time was measured using the first zero crossing in each pulse. Measurements were performed in room temperature water. Each measurement was repeated three times and the fragment was completely removed and replaced for each individual measurement. The average standard deviation across these three measurements was 2% [26].

F. Predicting Velocity with MR

The parameters derived from clinical MR imaging were correlated to the clinical HU value and the acoustic velocity measured in each fragment. The figure of merit for each correlation was the R-squared value.

G. Pore Structure and Velocity

Micro CT analysis of each fragment was used to study how pore structure contributes to acoustic velocity in a human skull. Specifically, each micro CT derived parameter was combined with HU to see if a two dimensional correlation resulted in a better prediction of acoustic velocity than HU alone. The primary figure of merit for this analysis was the R-squared value.

Further analysis was performed on eight fragments, selected because measurements detailed in Webb *et al.* [26] showed that they have similar average HU values but different velocities. These fragments were separated into two groups of four fragments each based on their velocity. The average velocity and CT HU of the fragments in each group is shown in Table I. A paired T-test was used to determine which Micro CT and T2-derived parameters could differentiate between the two groups.

III. Results

A. MR Based Prediction of Velocity

Figure 1 shows sample UTE, ZTE, and T2* images of fragments from the inner and outer tables and the medullary layer. For comparison, CT scans (80, 100, 120 and 140 kVp, bone plus kernel) are shown on the left. All of the images come from the same three fragments. Qualitatively, the MR images show an inverted contrast relative to the CT, with the cortical fragments from the inner and outer table appearing darker than the trabecular fragment from the medullary layer.

Figure 2 shows a quantitative comparison between HU and the ZTE and UTE magnitude and the mono-exponential T2* value of each fragment. All three parameters show a strong anti-correlation to HU. The HU used in these figures are obtained from CT images reconstructed with the Bone Plus kernel on the GE system using x-ray energies of 80, 100,

120, and 140 kVp. In all cases, both the slope and the y-intercept depend on the x-ray energy used to acquire the image. R-squared values are given in the legends and they average 0.80, 0.74, and 0.62 for the ZTE, UTE, and T2* values respectively. One fragment, a medullary piece with exceptionally large pores, was consistently an outlier and was excluded from the following analyses.

Figures 3(a) and 3(b) show the acoustic velocity plotted as a function of ZTE and UTE magnitude and Figure 3(c) shows the acoustic velocity as a function of the average T2* value for each fragment. The ZTE magnitude images provide the best estimate with an R-squared value of 0.39. Other R-squared values are shown in the legends.

B. Pore Structure and Acoustic Velocity

Figure 4 shows sample micro CT images of the eight fragments described in Table I. The top row of images corresponds to the high velocity group and the bottom row corresponds to the low velocity group.

Pore eccentricity improved estimates of velocity. As measured by the R-squared value, a linear combination of eccentricity and HU value accounts for 68% of the variation in velocity observed across the two skulls while clinical HU alone account for only 57%. Figure 5 compares these two conditions, using CT data acquired with the Veo reconstruction algorithm and an x-ray energy of 120 kVp. Figure 5(a) shows the correlation between HU alone and velocity and Figure 5(b) shows the simultaneous correlation of HU and eccentricity with velocity.

The improvement seen when eccentricity is included with HU was variable across the CT imaging methods. Like the Veo reconstruction, the dual energy images showed a substantial improvement in the R-squared value. The dual energy data was reconstructed at 5 energies [26] (60, 80, 100, 120, and 140 keV) and the average improvement in the R-squared value was 0.48 to 0.60. The images acquired with the Bone Plus kernel at 120 kVp showed only a modest increase from 0.46 to 0.51.

Unlike eccentricity, the combination of the other two micro-CT derived parameters (pore area and porosity) with the clinical HU value did not result in an improvement to the prediction of velocity (not shown).

A two tailed t-test shows that the eccentricity ($t(6)=-3.8$, $p<0.01$) and porosity ($t(6)=4.0$, $p<0.01$) of the two groups (see Table I) are significantly different. In contrast, pore area does not differentiate between the two groups ($t(6)=1.2$, $p=0.98$). The T2 spectrum differentiates between the two groups in several ways. Figure 6 shows the T2 spectra for these fragments, with the solid blue line corresponding to fragments from the high velocity group and the dotted red line corresponding to fragments from low velocity group. The most prominent differences between the groups occur in the locations of the peaks centered around 1s and 500μs (two-sided t-test, $t(6)=4.4$, $p<0.01$ and $t(6)=-3.7$, $p<0.01$ respectively). The difference in the locations of the peak centered around 0.3s is also significant (two-sided t-test, $t(6)=2.7$, $p<0.05$).

IV. Discussion

A. Predicting Velocity

This study demonstrates that MR can predict acoustic velocity with comparable but slightly less accuracy than CT (R-squared of 0.39 for ZTE images compared to 0.46 for the CT method currently used in the clinic and 0.52 for the best CT method according to [26]; compare Figure 3(a) to Figure 5(a)). MR-based bone imaging continues to evolve and future improvements may enable MR to replace CT as a planning modality for ablative treatments in the human brain. The ability to perform acoustic targeting without the need to acquire a CT would open the possibility of using ultrasound neuromodulation to study brain function in healthy volunteers and to treat pediatric patients.

MR may already be able to substitute for CT in applications where only the skull thickness is used to estimate phase corrections [30], [31]. For less invasive treatments - such as neuromodulation - MR is likely already capable of providing a sufficiently accurate estimate of acoustic velocity in individual patient skulls. However, these procedures lack the read-out of treatment efficacy provided by MR thermometry during ablation. Thus, further study is needed to characterize the accuracy with which either CT or MR can predict the acoustic intensity at focus. Existing studies find that while CT based simulation of intensity is well correlated within a single patient, CT based simulations fail to predict intensity across a patient population [42].

The capacity of relaxation time measurements to illuminate pore structure provides another mode through which MR can contribute to tcMRgFUS treatments. Figure 6 suggests that the relaxation time of pore water in fragments with higher eccentricity is more rapid than the relaxation time of pore water in fragments with lower eccentricity. This phenomenon is likely explained by differences in the surface area to volume ratio within these pores, with a higher ratio leading to a faster relaxation time. A clinical MR sequence that could measure this difference has the potential to improve CT or MR-based estimates of acoustic velocity.

Significant work remains to bring these results to the clinic. Micro CT measurements are not feasible in clinical settings. Thus, while the eccentricity results offer insight into what data is missing from the transformation between clinical HU values and velocity, they do not provide a clinically relevant method to improve this transformation. Similarly, the detailed T2 spectra would be difficult to obtain *in-vivo* and the ability of the spectrum to differentiate between the two groups does not guarantee that T2 derived parameters will improve the overall estimate. Thus, further work is needed to validate the efficacy of T2 as a predictor of acoustic velocity.

Future studies will also need to address limitations resulting from the difference between re-hydrated *ex-vivo* fragments and *in-vivo* measurements. Specifically, voxels spanning the skull and skin or skull and brain will likely require a different transformation between the measured imaging parameter and acoustic velocity. Thus, the actual *in-vivo* resolution will affect the accuracy of the estimate at the skull edges. The presence of blood, skin, and marrow will impact T2 and T2* measurements. Future T2 or T2* based studies should look

for clinically relevant compromises between the single exponential measurement presented in Figure 3(c) and the detailed spectra given in Figure 6.

Our results agree with other studies that suggest that the role of pore structure in determining acoustic velocity is significant but small [35], [36]. For some of the CT reconstructions, including eccentricity substantially improved the accuracy of velocity estimates. Notably, the reconstructions most improved by including eccentricity were the reconstructions that already provided the best predictions. Other reconstructions showed only a minimal change when eccentricity was included. Thus, including pore structure in velocity estimates is only one aspect of the difficulty of estimating acoustic velocity with electromagnetic waves.

Using ultrasound to measure acoustic velocity directly offers a potential alternative to CT/MR as a method of determining acoustic velocity in a patient's skull. QUS measurements in femur and tibia have been shown to provide information about both the thickness and velocity of cortical bone [43]. An extension of these methods to the skull may offer a direct measurement of acoustic phase, eliminating the need to transform measurements from one modality to another.

B. Theoretical Interpretation

Models that rely on HU to predict velocity generally rely on the ability of HU to estimate the fraction of water and bone composing each voxel. The Aubry model [24] makes this explicit, transforming HU into a porosity metric that varies from 0 to 1. The speed of sound in the skull can then be estimated as a linear combination of the acoustic velocity in water and in cortical bone, with the linear coefficients selected based on the porosity.

Other models, such as the Pichardo [25] and Connor [23] models, don't rely explicitly on porosity to estimate velocity. These models are derived using an optimization that allows for an arbitrary relationship between HU and velocity. Of course, the models are still limited by the information contained in the HU value of each voxel.

Missing from HU is information about shape and orientation of pores in the bone. CT is capable of capturing this information but at the current resolution of clinical scanners this structure is lost. To understand how this information contributes to velocity, consider the equation giving the speed of sound in solids. Neglecting the shear modulus, the speed of sound in a solid is given by [44]

$$c = \frac{1}{\sqrt{\kappa \rho}}, \tag{2}$$

where κ is the compressibility of the bone and ρ is the density. Density is well approximated by HU because it is independent of the structure of the pores. In contrast, κ depends heavily on both the porosity of a voxel and the pore structure within that voxel. CT only captures part of this information because it is only effected by the raw volume of calcified bone, blood, and marrow and it is not effected by the shape of pores. For pores smaller than the resolution of the image, the HU value is also not effected by the size of the pores (i.e. within a single voxel many small pores could result in the same HU value as a single larger pore).

The contribution of pore structure to compressibility is particularly relevant at low frequencies such as 500 kHz where the wavelength is large relative to the pore structure. At these frequencies, a single wavelength spans multiple pores and the acoustic energy therefore sees a compressibility that depends on the pore structure. The improvement shown in Figure 5 provides evidence that pore shape can change the compressibility of the bone, providing evidence that HU alone are not able to accurately predict the velocity across fragments with varying pore eccentricity. When information about pore shape is added, however, the accuracy of the velocity estimate improves substantially. This suggests that macro structure as well as composition need to be accounted for in order to obtain accurate velocity estimates, particularly across a patient population.

Simulation studies in the femur [35]also suggest that pore structure contributes significantly to the acoustic velocity in bone. Similar simulation studies in skull fragments should be done to further illuminate the tissue properties that must be identified to achieve accurate prediction of the acoustic velocity in a particular patient's skull.

V. Conclusion

This study provides strong evidence that pore structure contributes significantly to the acoustic velocity of skull bone, demonstrating that measurements of pore shape can improve the accuracy of acoustic velocity estimates. The ability of MR to provide quantitative estimates of velocity and to differentiate between high and low eccentricity samples suggests that MR has the potential to play an even larger role in treatment planning for tcMRgFUS procedures. CT-based estimates of acoustic velocity already enable several acoustic therapies in the human brain. Further improvements to the accuracy of these estimates will lead to higher spatial precision and the ability to reach therapeutic intensities at the target region with less acoustic power, resulting in safer and more effective treatments.

Acknowledgments

CT measurements were performed with the help of Lior Molvin. Oscilloscope measurements were performed on an instrument donated by Keysight Technologies. we also wish to acknowledge funding support from NIH Grant #s R01 MH111825, PO1 CA159992, the FUS Foundation, GE Healthcare, and InSightec.

References

[1]. Magara A, Bühler R, Moser D, Kowalski M, Pourtehrani P, and Jeanmonod D, "First experience with MR-guided focused ultrasound in the treatment of Parkinson's disease," Journal of Therapeutic Ultrasound, vol. 2, no. 11, pp. 1–8, 2014. [Online]. Available: [PubMed: 25516803]

[2]. Na YC, Chang WS, Jung HH, Kweon EJ, and Chang JW, "Unilateral Magnetic Resonance-Guided Focused Ultrasound Pallidotomy For Parkinson Disease," Neurology, vol. 85, no. 6, pp. 549–552, 2015. [PubMed: 26180137]

[3]. Elias WJ, Huss D, Voss T, Loomba J, Khaled M, Zadicario E, Frysinger RC, Sperling SA, Wylie S, Monteith SJ, Druzgal J, Shah BB, Harrison M, and Wintermark M, "A pilot study of focused ultrasound thalamotomy for essential tremor." The New England Journal of Medicine, vol. 369, no. 7, pp. 640–648, 2013. [Online]. Available: [PubMed: 23944301]

[4]. Jeanmonod D, Werner B, Morel A, Michels L, Zadicario E, Schiff G, and Martin E, "Transcranial magnetic resonance imaging guided focused ultrasound: noninvasive central lateral thalamotomy for chronic neuropathic pain," Neurosurgical Focus, vol. 32, no. 1, p. E1, jan 2012. [Online]. Available:

[5]. Jung HH, Kim SJ, Roh D, Chang JG, Chang WS, Kweon EJ, Kim C.-h., and Chang JW, "Bilateral thermal capsulotomy with MR-guided focused ultrasound for patients with treatment-refractory obsessive-compulsive disorder: a proof-of-concept study," Molecular Psychiatry, vol. 20, no. 10, pp. 1205–1211, oct 2015. [Online]. Available: [PubMed: 25421403]

[6]. Huang Y, Alkins R, Schwartz ML, and Hynynen K, "Opening the Blood-Brain Barrier with MR Imaging-guided Focused Ultrasound : Preclinical Testing on a Trans-Human Skull Porcine Model," Radiology, vol. 282, no. 1, pp. 123–130, 2017. [PubMed: 27420647]

[7]. Hynynen K, McDannold N, Vykhodtseva N, and Jolesz FA, "Noninvasive MR imaging-guided focal opening of the blood-brain barrier in rabbits." Radiology, vol. 220, no. 3, pp. 640–646, sep 2001. [Online]. Available: [PubMed: 11526261]

[8]. Choi JJ, Pernot M, Small SA, and Konofagou EE, "Noninvasive, Transcranial and Localized Opening of the Blood-Brain Barrier Using Focused Ultrasound in Mice," Ultrasound in Medicine & Biology, vol. 33, no. 1, pp. 95–104, 2007. [PubMed: 17189051]

[9]. McDannold N, Arvanitis CD, Vykhodtseva N, and Livingstone MS, "Temporary disruption of the blood-brain barrier by use of ultrasound and microbubbles: safety and efficacy evaluation in rhesus macaques," Cancer Research, vol. 72, no. 14, pp. 3652–3663, 2012. [PubMed: 22552291]

[10]. Lipsman N, Ironside S, Alkins R, Bethune A, Huang Y, Perry J, Sahgal A, Trudeau M, Hynynen K, and Mainprize T, "Initial Experience Of Blood-Brain Barrier Opening For Chemotherapeutic-Drug Delivery To Brain Tumurs By MR-Guided Focused Utrasound," Neuro-Oncology, vol. 19, no. suppl_6, pp. vi275–vi275, nov 2017. [Online]. Available:

[11]. Lee W, Lee SD, Park MY, Foley L, Purcell-Estabrook E, Kim H, Fischer K, Maeng L.-s., and Yoo S.-s., "Image-Guided Focused Ultrasound-Mediated Regional Brain Stimulation in Sheep," Ultrasound in Medicine & Biology, vol. 42, no. 2, pp. 459–470, 2016. [PubMed: 26525652]

[12]. Ye PP, Brown JR, and Pauly KB, "Frequency dependence of ultrasound neurostimulation in the mouse brain," Ultrasound in Medicine and Biology, vol. 42, no. 7, pp. 1512–1530, 2016. [PubMed: 27090861]

[13]. Kamimura HAS, Wang S, Chen H, Wang Q, Aurup C, Acosta C, Carneiro AAO, and Konofagou EE, "Focused ultrasound neuromodulation of cortical and subcortical brain structures using 1.9 MHz," Medical Physics, vol. 43, no. 10, pp. 5730–5735, 2016. [Online]. Available: [PubMed: 27782686]

[14]. King RL, Brown JR, and Butts Pauly K, "Localization of Ultrasound-Induced In Vivo Neurostimulation in The Mouse Model," Ultrasound in medicine & biology, vol. 40, no. 7, pp. 1512–1522, 2014. [PubMed: 24642220]

[15]. King RL, Brown JR, Newsome WT, and Butts Pauly K, "Effective Parameters for Ultrasound-Induced In Vivo Neurostimulation," Ultrasound in medicine & biology, vol. 39, no. 2, pp. 312–331, 2013. [PubMed: 23219040]

[16]. Yoo S-S, Bystritsky A, Lee J-H, Zhang Y, Fischer K, Min B-K, McDannold NJ, Pascual-Leone A, and Jolesz FA, "Focused ultrasound modulates region-specific brain activity," NeuroImage, vol. 56, no. 3, pp. 1267–1275, jun 2011. [Online]. Available: [PubMed: 21354315]

[17]. Tufail Y, Matyushov A, Baldwin N, Tauchmann ML, Georges J, Yoshihiro A, Tillery SIH, and Tyler WJ, "Transcranial Pulsed Ultrasound Stimulates Intact Brain Circuits," Neuron, vol. 66, no. 5, pp. 681–694, 2010. [Online]. Available: [PubMed: 20547127]

[18]. Dallapiazza RF, Timbie KF, Holmberg S, Gatesman J, Lopes MB, Price RJ, Miller GW, and Elias WJ, "Noninvasive neuromodulation and thalamic mapping with low-intensity focused ultrasound," Journal of Neurosurgery, vol. 128, no. 3, pp. 875–884, mar 2018. [Online]. Available: [PubMed: 28430035]

[19]. Deffieux T, Younan Y, Wattiez N, Tanter M, and Pouget P, "Low-Intensity Focused Ultrasound Modulates Monkey Visuomotor Behavior," Current Biology, vol. 23, no. 23, pp. 2430–2433, 2013. [PubMed: 24239121]

[20]. Lee W, Kim H, Jung Y, Song I.-u., Chung YA, and Yoo S.-s., "Image-Guided Transcranial Focused Ultrasound Stimulates Human Primary Somatosensory Cortex," Scientific Reports, vol. 5, no. 1, p. 8743, aug 2015. [Online]. Available: [PubMed: 25735418]

[21]. Legon W, Sato TF, Opitz A, Mueller J, Barbour A, Williams A, and Tyler WJ, "Transcranial focused ultrasound modulates the activity of primary somatosensory cortex in humans." Nature neuroscience, vol. 17, no. 2, pp. 322–329, jan 2014. [Online]. Available: [PubMed: 24413698]

[22]. Mueller J, Legon W, Opitz A, Sato TF, and Tyler WJ, "Transcranial focused ultrasound modulates intrinsic and evoked EEG dynamics," Brain Stimulation, vol. 7, no. 6, pp. 900–908, 2014. [Online]. Available: [PubMed: 25265863]

[23]. Connor CW, Clement GT, and Hynynen K, "A unified model for the speed of sound in cranial bone based on genetic algorithm optimization." Physics in Medicine and Biology, vol. 47, no. 22, pp. 3925–3944, 2002. [PubMed: 12476974]

[24]. Aubry J-F, Tanter M, Pernot M, Thomas J-L, and Fink M, "Experimental demonstration of noninvasive transskull adaptive focusing based on prior computed tomography scans," The Journal of the Acoustical Society of America, vol. 113, no. 1, pp. 84–93, jan 2003. [Online]. Available: [PubMed: 12558249]

[25]. Pichardo S, Sin VW, and Hynynen K, "Multi-frequency characterization of the speed of sound and attenuation coefficient for longitudinal transmission of freshly excised human skulls," Physics in Medicine and Biology, vol. 56, no. 1, pp. 219–250, jan 2011. [Online]. Available: [PubMed: 21149950]

[26]. Webb TD, Leung SA, Rosenberg J, Ghanouni P, Dahl JJ, Pelc NJ, and Pauly KB, "Measurements of the Relationship between CT Hounsfield Units and Acoustic Velocity and How It Changes with Photon Energy and Reconstruction Method," IEEE Transactions on Ultrasonics, Ferroelectrics, and Frequency Control, vol. 65, no. 7, pp. 1111–1124, 2018. [PubMed: 29993366]

[27]. Ghanouni P, Pauly KB, Elias WJ, Henderson J, Sheehan J, Monteith S, and Wintermark M, "Transcranial MRI-guided focused ultrasound: A review of the technologic and neurologic applications," American Journal of Roentgenology, vol. 205, no. 1, pp. 150–159, 2015. [PubMed: 26102394]

[28]. Jung HH, Chang WS, Rachmilevitch I, Tlusty T, Zadicario E, and Chang JW, "Different Magnetic Resonance Imaging Patterns After Transcranial Magnetic Resonance-Guided Focused Ultrasound of the Ventral Intermediate Nucleus of the Thalamus and Anterior Limb of the Internal Capsule in Patients with Essential Tremor or Obsessive-Comp," Journal of Neurosurgery, vol. 122, no. 1, pp. 162–168, 2015. [PubMed: 25343176]

[29]. Johnson EM, Vyas U, Ghanouni P, Pauly KB, and Pauly JM, "Improved cortical bone specificity in UTE MR Imaging," Magnetic Resonance in Medicine, vol. 77, no. 2, pp. 684–695, 2017. [PubMed: 26972442]

[30]. Wiesinger F, Sacolick LI, Menini A, Kaushik SS, Ahn S, Veit-Haibach P, Delso G, and Shanbhag DD, "Zero TE MR bone imaging in the head," Magnetic Resonance in Medicine, vol. 75, no. 1, pp. 107–114, 2016. [PubMed: 25639956]

[31]. Wiesinger F, Bylund M, Yang J, Kaushik S, Shanbhag D, Ahn S, Jonsson JH, Lundman JA, Hope T, Nyholm T, Larson P, and Cozzini C, "Zero TE-based pseudo-CT image conversion in the head and its application in PET/MR attenuation correction and MR-guided radiation therapy planning," Magnetic Resonance in Medicine, no. January, pp. 1–12, 2018. [Online]. Available:

[32]. Grimal Q and Laugier P, "Quantitative ultrasound assessment of cortical bone properties beyond bone mineral density," IRBM, vol. 40, no. 1, pp. 16–24, 2019. [Online]. Available:

[33]. Bernard S, Schneider J, Varga P, Laugier P, Raum K, and Grimal Q, "Elasticity-density and viscoelasticity–density relationships at the tibia mid-diaphysis assessed from resonant ultrasound spectroscopy measurements," Biomechanics and Modeling in Mechanobiology, vol. 15, no. 1, pp. 97–109, 2016. [PubMed: 26070349]

[34]. Haïat G, Padilla F, Peyrin F, and Laugier P, "Variation of ultrasonic parameters with microstructure and material properties of trabecular bone: A 3d model simulation," Journal of Bone and Mineral Research, vol. 22, no. 5, pp. 665–674, 2007. [Online]. Available: [PubMed: 17295606]

[35]. Grimal Q, Rohrbach D, Grondin J, Barkmann R, Glüer C-C, Raum K, and Laugier P, "Modeling of femoral neck cortical bone for the numerical simulation of ultrasound propagation," Ultrasound in Medicine & Biology, vol. 40, no. 5, pp. 1015–1026, 2014. [Online]. Available: [PubMed: 24486239]

[36]. Rohde K, Rohrbach D, Glüer C-C, Laugier P, Grimal Q, Raum K, and Barkmann R, "Influence of porosity, pore size, and cortical thickness on the propagation of ultrasonic waves guided through the femoral neck cortex: a simulation study," IEEE Transactions on Ultrasonics, Ferroelectrics, and Frequency Control, vol. 61, no. 2, pp. 302–313, 2014. [PubMed: 24474136]

[37]. Peralta L, Maeztu Redin JD, Fan F, Cai X, Laugier P, Schneider J, Raum K, and Grimal Q, "Bulk wave velocities in cortical bone reflect porosity and compression strength," Ultrasound in Medicine & Biology, vol. 47, no. 3, pp. 799–808, 2021. [Online]. Available: [PubMed: 33341302]

[38]. Raum K, Leguerney I, Chandelier F, Bossy E, Talmant M, Saïed A, Peyrin F, and Laugier P, "Bone microstructure and elastic tissue properties are reflected in qus axial transmission measurements," Ultrasound in Medicine & Biology, vol. 31, no. 9, pp. 1225–1235, 2005. [Online]. Available: [PubMed: 16176789]

[39]. Horch RA, Nyman JS, Gochberg DF, Dortch RD, and Does MD, "Characterization of 1H NMR signal in human cortical bone for magnetic resonance imaging," Magnetic Resonance in Medicine, vol. 64, no. 3, pp. 680–687, 2010. [Online]. Available: [PubMed: 20806375]

[40]. Otsu N, "A Threshold Selection Method from Gray-Level Histograms," IEEE Transactions on Systems, Man, and Cybernetics, vol. 9, no. 1, pp. 62–66, 1979.

[41]. Sollie P, Morphological Image Analysis: Principles and Applications. Springer-Verlag, 1999.

[42]. Leung SA, Webb TD, Bitton RR, Ghanouni P, and Butts Pauly K, "A rapid beam simulation framework for transcranial focused ultrasound," Scientific reports, vol. 9, no. 1, p. 7965, 2019. [PubMed: 31138821]

[43]. Iori G, Du J, Hackenbeck J, Kilappa V, and Raum K, "Estimation of cortical bone microstructure from ultrasound backscatter," IEEE Transactions on Ultrasonics, Ferroelectrics, and Frequency Control, vol. 68, no. 4, pp. 1081–1095, 2021. [PubMed: 33104498]

[44]. Szabo TL, Diagnostic Ultrasound Imaging: Inside Out, 2nd ed. Amsterdam, The Netherlands: Elsevier, 2014. [Online]. Available:

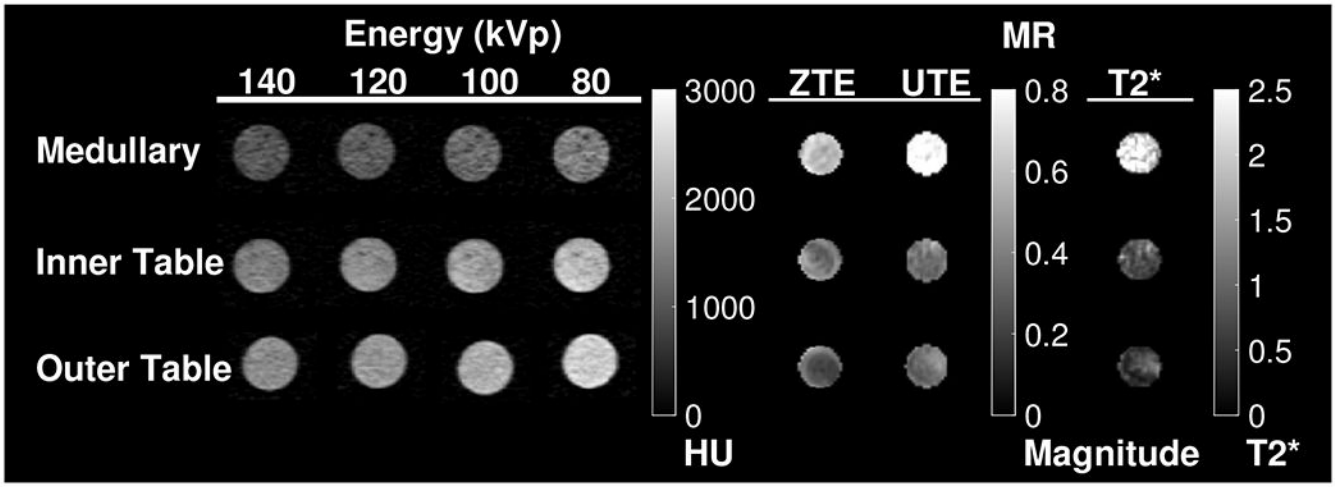

Fig. 1.

Images of a fragment from the inner table, the medullary, and the outer table. From left to right the figure shows images from CT scans using x-ray energies of 140, 120, 100, and 80 kVp, magnitude images from a ZTE and UTE MR scan and T2* reconstructions. The brightness of the CT image depends on the x-ray energy and cortical fragments are brighter than trabecular fragments. The MR images follow the reverse pattern, with the cortical fragments being dim relative to the medullary fragment.

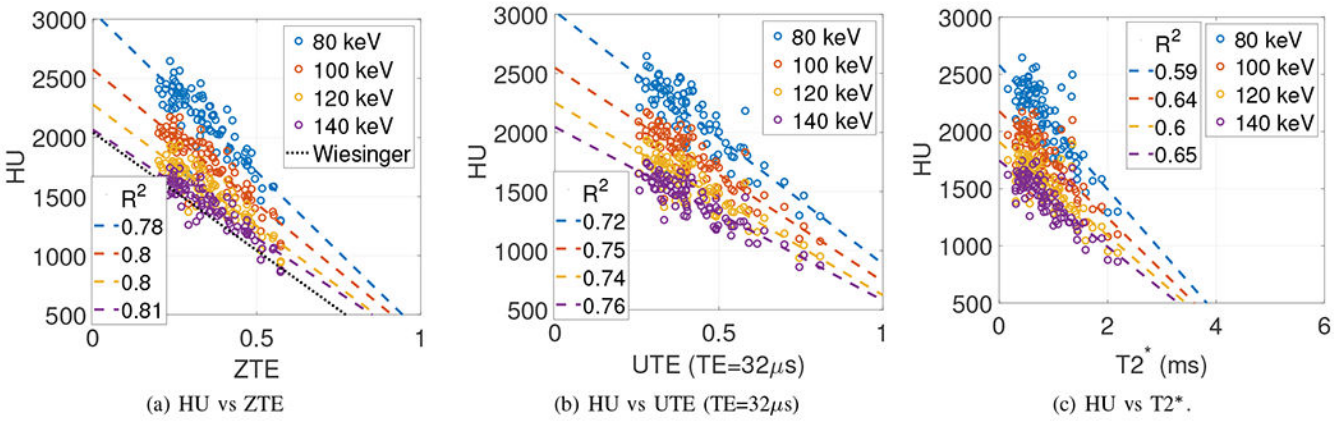

(a) HU vs ZTE (b) HU vs UTE (TE=32μs) (c) HU vs T2*.

Fig. 2.

A comparison of CT and MR imaging for each fragment. In each plot the average HU value is shown as a function of the a) ZTE magnitude, b) UTE magnitude, and c) the mono exponential T2* reconstruction. CT values were obtained using the Bone Plus kernel on the GE system

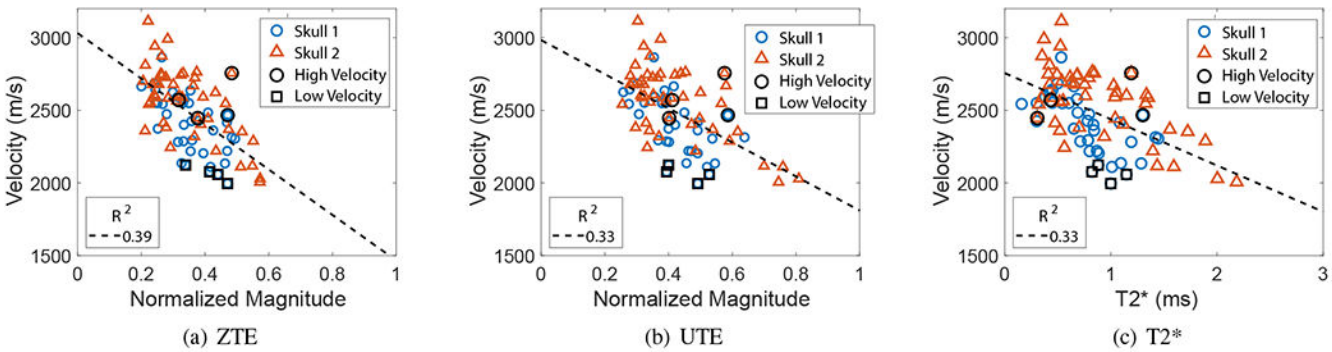

Fig. 3.

Acoustic velocity plotted as a function of ZTE (a) and UTE (b) magnitude and as a function of T2* (c). Fragments from the high velocity group are marked with black circles and fragments from the low velocity group are marked with black squares.

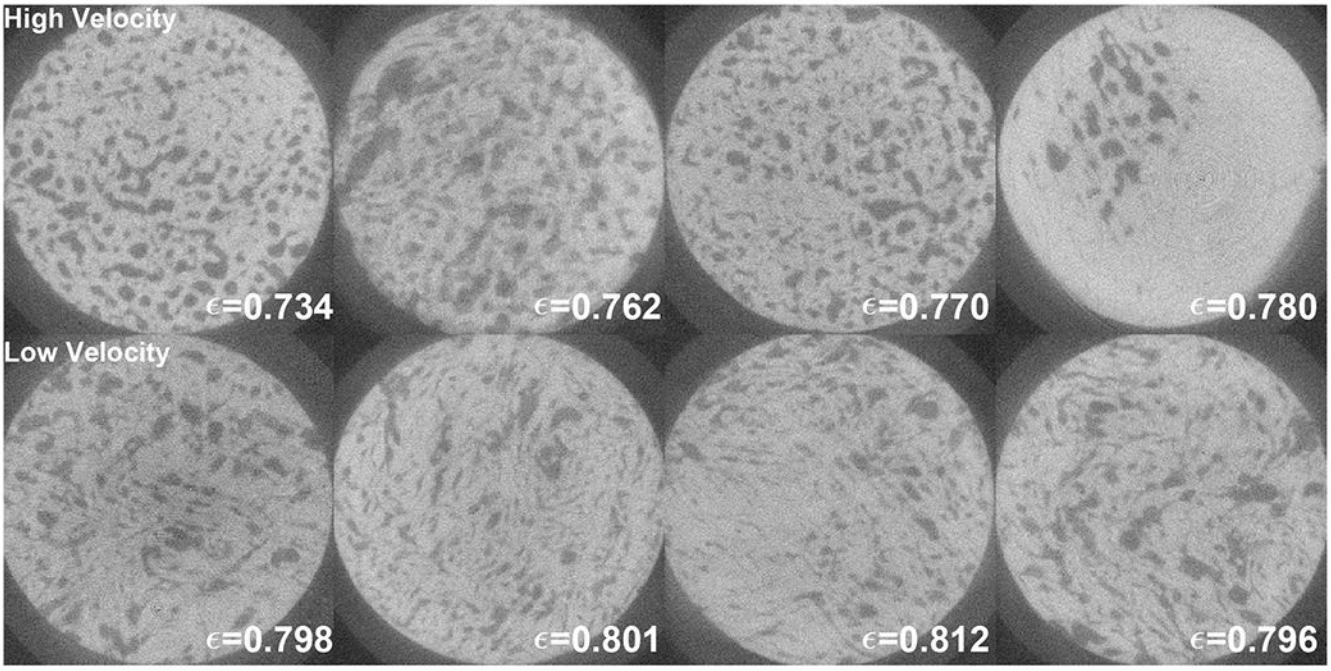

Fig. 4.

Images and average eccentricity values of the fragments from the high (top row) and low (bottom row) velocity groups.

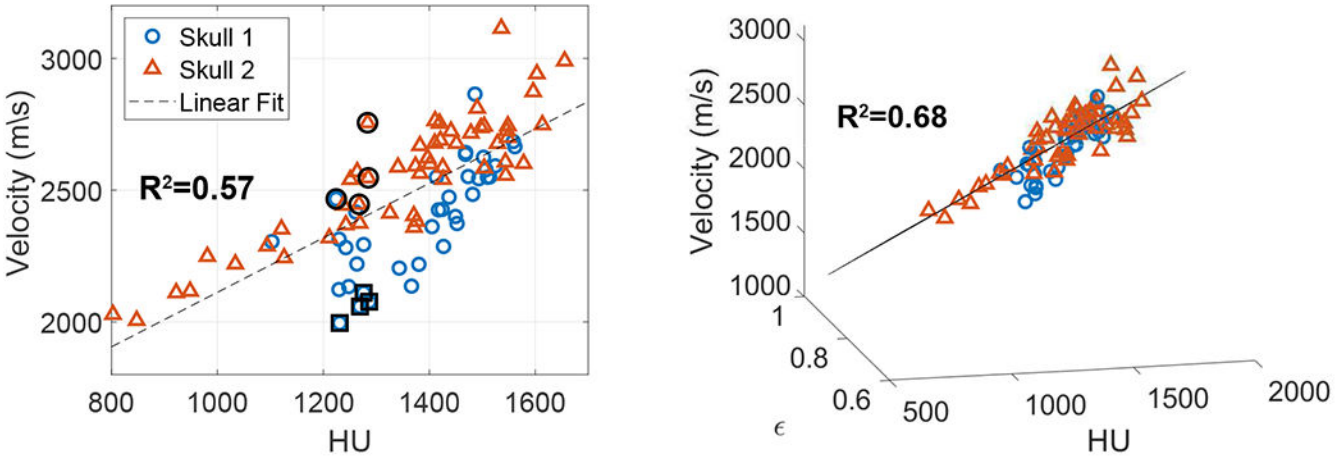

(a) Velocity as a function of HU alone

(b) Velocity as a function of HU and eccentricity

Fig. 5.

Acoustic velocity plotted as a function of clinical HU alone [26] (a) and as a function of both clinical HU and eccentricity. The HU values were acquired using an x-ray energy of 120 kVp and the VEO reconstruction technique on the GE scanner.

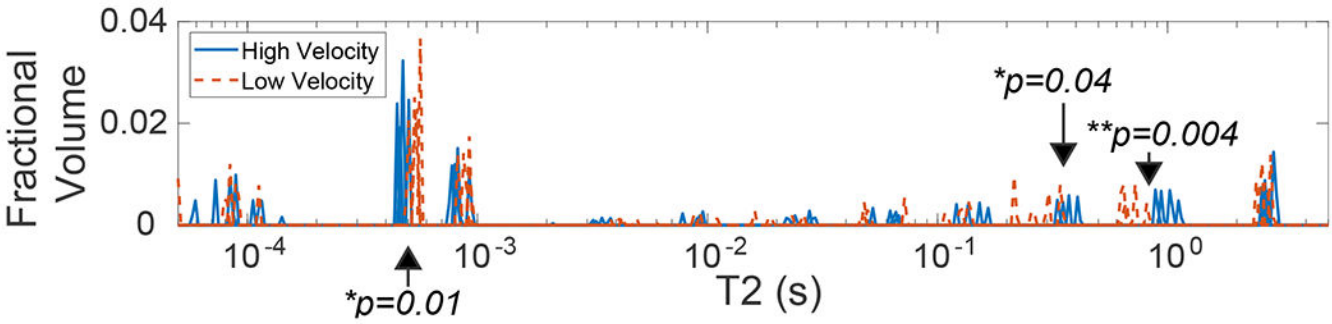

Fig. 6.

T2 spectra measured in the high velocity (blue) and low velocity (dotted red) groups. When separated according to which velocity group the fragment comes from, there is a significant difference between the locations of the peak centered at 500μs, 0.3s, and 1s (arrows).

TABLE I

GROUPS OF FRAGMENTS WITH SIMILAR HU VALUES BUT DIFFERENT VELOCITIES

Group	Avg. Velocity	Avg. HU
High Velocity	2554 m/s	1265
Low Velocity	2060 m/s	1266